Program Final Report
PFR-3243

Microhydraulic Actuators for Microrobotics

J. T. Kedzierski

31 March 2022

Lincoln Laboratory
MASSACHUSETTS INSTITUTE OF TECHNOLOGY
LEXINGTON, MASSACHUSETTS

This material is based upon work supported by the Under Secretary of Defense for Research and Engineering and Defense Advanced Research Projects under Air Force Contract No. FA8702-15-D-0001.

This report is the result of studies performed at Lincoln Laboratory, a federally funded research and development center operated by Massachusetts Institute of Technology. This material is based upon work supported by the Under Secretary of Defense for Research and Engineering and Defense Advanced Research Projects Agency under Air Force Contract No. FA8702-15-D-0001. Any opinions, findings, conclusions or recommendations expressed in this material are those of the author(s) and do not necessarily reflect the views of the Under Secretary of Defense for Research and Engineering and Defense Advanced Research Projects Agency.

Massachusetts Institute of Technology
Lincoln Laboratory

Microhydraulic Actuators for Microrobotics

Kedzierksi, Jakub T.
Group 81

Program Final Report PFR-3243

30 March 2022

This material is based upon work supported by the Under Secretary of Defense for Research and Engineering
And Defense Advanced Research Projects under Air Force Contract No. FA8702-15-D-0001.

Lexington Massachusetts

ABSTRACT

Electrostatic motors have traditionally suffered from high voltage and low torque, leaving them with a vanishingly small portion of the motor application space. The lack of a robust electrostatic motor technology is of particular concern in microsystems, because inductive motors do not scale well to small dimensions. Often microsystem designers have to choose from a host of imperfect actuation solutions, leading to high voltage requirements or low efficiency and thus straining the power budget of the entire system. In this work we describe a scalable three-dimensional actuator technology that is based on the stacking of thin microhydraulic layers. This technology offers an actuation solution at 50 volts, with high force, high efficiency, fine stepping precision, layering, low abrasion, and resistance to pull-in instability. Actuator layers can also be stacked in different configurations trading off speed for force, and improve quadratically in power density when the internal dimensions are scaled down.

This material is based upon work supported by the Under Secretary of Defense for Research and Engineering and Defense Advanced Research Projects Agency under Air Force Contract No. FA8702-15-D-0001. Any opinions, findings, conclusions or recommendations expressed in this material are those of the author(s) and do not necessarily reflect the views of the Under Secretary of Defense for Research and Engineering and Defense Advanced Research Projects Agency

TABLE OF CONTENTS

LIST OF ILLUSTRATIONS

Figure No. **Page**

1. INTRODUCTION

The invention of electrostatic motors, pioneered by Benjamin Franklin and Andrew Gordon in 1740, significantly predates Michael Faraday's demonstration of the first inductive motor in 1821, yet electrostatic motors have never gained a significant technological foothold. Historically, electrostatic motors require high voltage and have low output power. In the last few decades microelectromechanical (MEMS) motors [1] improved the outlook for capacitively driven rotational actuation. At a micro-scale higher driving frequency can increase power density, and smaller electrode gaps can reduce driving voltage. Some high-frequency piezoelectrically driven ultrasonic motors [2,3] have gained commercial acceptance, however most MEMS motors still suffer from unacceptably low torque, and the inability to scale in three dimensions due to their inherently thin nature [4]. To address these challenges a desirable electrostatic motor technology should offer low-voltage, high-torque, high-efficiency, and the ability to scale up in thickness. It is known how to achieve these characteristics individually. Low voltage operation can be obtained by using a thin dielectric [5,6]. High torque can be obtained by having a large capacitance change in a small displacement, either by using planar capacitive coupling [5,7], or by using a small stepping distance [5,8,9]. Extendibility in thickness, without increasing voltage, can be obtained with a layered structure design [10,11]. And high-efficiency can be obtained by using a dielectric with low loss [5,8,12]. All these characteristic have been individually demonstrated, but to our knowledge they have never been combined into one actuator technology.

In this work we demonstrate such a technology by extending microhydraulic electrowetting actuators [5,13], which already demonstrate low-voltage, high-torque density, and high-efficiency, into the third dimension by layering multiple actuating films into a single unit. Microhydraulic technology works by electrically distorting the equilibrium surface tension state of attached liquid droplets with electrowetting [14,15,16,17]. In previous work, droplet arrays on a thin film of polyimide [5,13] were actuated by a dielectric covered electrode array on top of a thick base. In order to extend this technology in three dimensions we have integrated the electrode and droplet arrays into one thin film, with the droplet array on one side and the electrode array on the other. The resulting layers can be stacked, and individually powered throughout the stack with a liquid interconnect network [18,19]. In addition to high-torque, low-voltage, efficiency, and stacking, our actuators have four other desirable qualities. One, all solid moving components are separated by a fluidic layer and never come into direct contact, thus avoiding stiction and abrasion issues common in MEMs motors [20]. Two, the dielectric is rigid, thus the electric field during actuation remains largely constant for charged regions, avoiding pull-in instability issues that cause breakdown in compliant dielectric actuators [21]. Three, as will be shown in this work, different configurations can be used to internally gear the actuator, trading off speed for torque as applications demand. And four, power and force densities scale quadratically as the internal size scale of the actuator is reduced, giving it a Moore's Law like scaling advantage [5]. Even with the modest droplet pitch of 40 μm, we demonstrate a power density similar to inductive motors at much higher torque. Scaling to a 15 μm pitch gives roughly another order of magnitude in force and power. Due to this unique combination of characteristics, multilayer microhydraulic actuators could foster future advances in responsive robotic joints, microrobotics, and robotic surgery.

2. RESULTS

2.1 STRUCTURE

This section focuses on the rotational actuator, although linear actuators were built in a similar manner. Actuators consisted of staked 10 µm thick layers of polyimide separated by fluid. Figure 1 shows a detailed view of a single rotational layer, viewed from the droplet and electrode sides. The droplet side, shown in Figure 1abd, consisted of hydrophilic and hydrophobic solid surfaces, with hydrophilic areas wetted by water containing 8 M LiCl, forming semi-cylindrical structured droplets. Uniform Laplace pressure gave connected droplets a specific curvature, as shown in Figure 1de. The two types of droplets, radial and circumferential, served different functions. The radial "drive" droplets were responsible for inter-layer motion when distorted by electrowetting forces, and formed the 330 (N_{drop}) unit circular droplet array. The circumferential "rail" droplets formed the 3 inner and 3 outer rails, which carried the electrical signals for the phases P1-P4, and the drive droplet reference potential R. At the edges of all droplets there was a wall of polyimide to increase the droplet height and reduce viscous effects during actuation. The electrode side, shown in Figure 1ce, consisted of 2 metal layers and an electrowetting dielectric. The inner Pt metal layer formed the electrode brushes, and connected the rail droplets to the drive electrodes. The outer Al metal layer formed the drive electrodes. A 1.1 µm layer of polyimide topped with 14 nm of fluoropolymer formed the surface electrowetting dielectric. Holes in the film at the rails formed the fluidic vias when wetted, and were the only non-planer feature on the electrode side, as shown in Figure 1e. The four phases of the drive electrodes alternated from P1 to P4 in a counter-clockwise manner for regular electrode order layers, and in a clockwise manner for inverted electrode order layers. Each unit of four electrodes and one drive droplet formed a cycle segment of the actuator, giving 330 cycles for a complete rotation, and 1340 driving electrodes per rotational layer. The length of cycle segment was one droplet pitch (D_{pitch}), of 1.09°, or approximately 40 µm in the middle of the array. Layers were marked with an identifying number at the tab, as shown in Figure 1a. An R after the identifying number indicated an inverted electrode order. Finally there were two special layers, the base and the top. The base had no driving electrodes or driving droplets, and consisted only of the 6 rails and external electrical connections. The top layer had no driving electrodes with only a logo text in the metal layer, and was labeled as T in the tab.

The stacked layer structure of a 5 layer rotational actuator is shown in Figure 2, with a base layer at the bottom, and a top layer on top. The first layer was stacked on the base, droplet side to droplet side, with the water rails bridged for each phase. Subsequent layers were stacked droplet side to electrode side, with the fluidic rails aligning to the fluidic vias of the layer below, and the driving droplets aligning to the driving electrodes. Surface tension forces between vias and rails self-aligned the layers into translational alignment [22], while rotational alignment was achieved when P2, and P3 were held high, typically 30 V. Before self-alignment was possible layers had to be manually aligned to within half rail pitch (40 µm) translationally, and within half cycle angle (0.6°) rotationally. After self-alignment the translational misalignment was less than 1 µm, and rotational less than 0.03°.

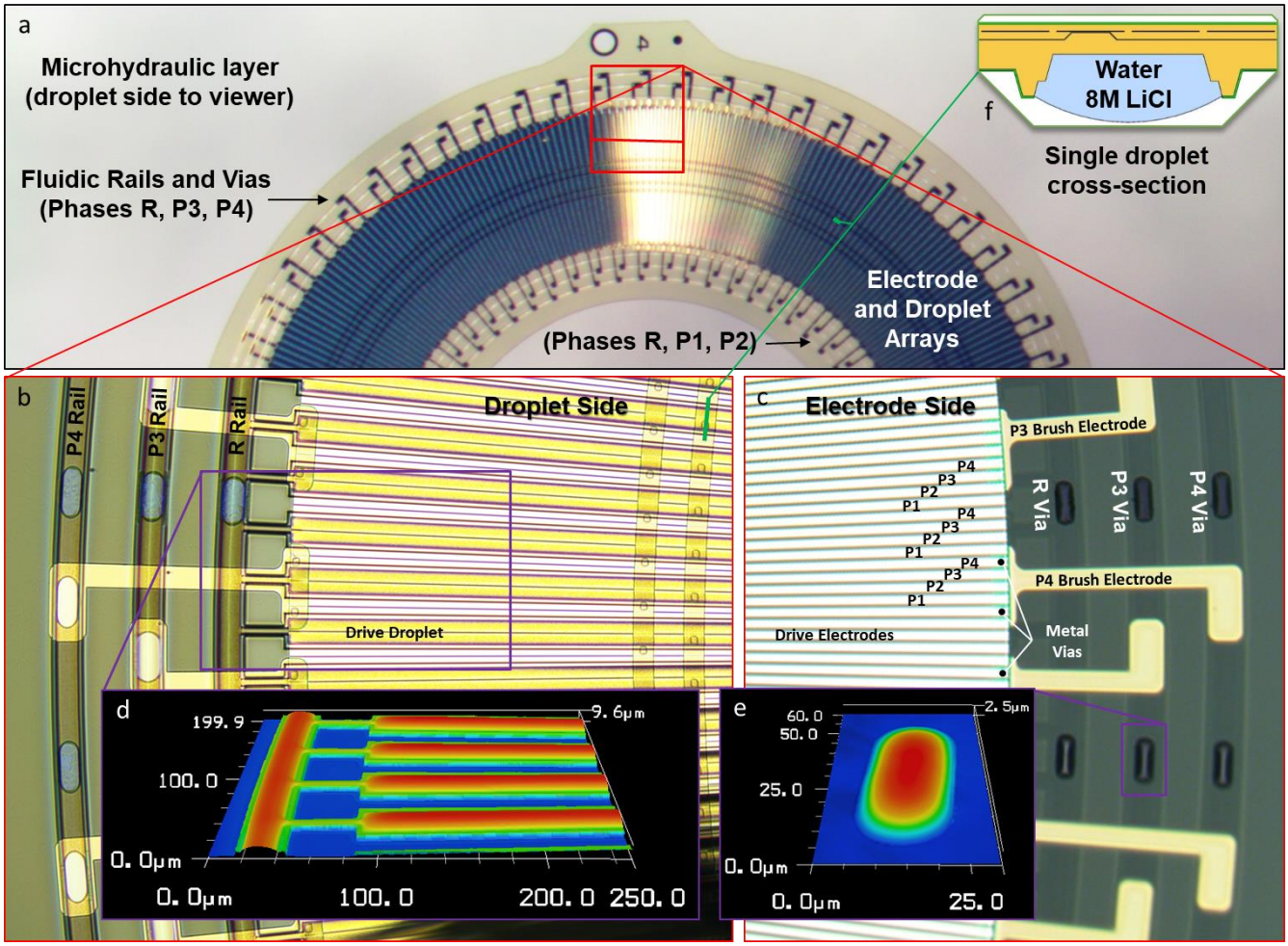

Figure 1. A detailed view of a single microhydraulic rotational layer. ***(a)*** *Shows a low magnification picture taken from the droplet side, showing the outside rails, inside rails, the droplet array, and the electrode array.* ***(b)*** *Shows a magnified view of the droplet side with the drive droplets and outside rails. Features on the electrode side are also visible since polyimide and water are transparent.* ***(c)*** *Shows the electrode side with the four phase Al drive electrodes, and the Pt brush electrodes.* ***(d)*** *Shows the confocal microscope height map of the droplet side, showing the surface curvature of the drive and rail droplets as well as the edge of the droplet wall.* ***(e)*** *Shows a height map of the fluidic via from the electrode side. Liquid profiles on both sides have a radius curvature of approximately 18 µm, which corresponds to a Laplace pressure of 3.8 kPa or 31 cm of 8M LiCl with the air/water surface tension. Curvature is similar to that caused by the 24 cm of 8M LiCl used in the fabrication of the actuator with the oil/water surface tension. A cross section diagram of a cycle section of the actuator is shown in* ***(f)****.*

2.2 OPERATION

Actuators operated by sending quarter-cycle offset trapezoidal signals, at a frequency F_{cyc}, to the four phases, P1-4, and holding R at a fixed zero or negative potential, as described in previous work for non-stacked actuators [5]. Each signal edge resulted in a single step of the actuator over an electrode. A cycle consisted of four steps and resulted in a relative movement by D_{pitch}. An electrical phase sequence of P1-4 resulted in motion in one direction, while the electrical phase sequence of P4-1 resulted in actuator motion in the other direction. Since all layers shared the same rail network, the electrical phase sequence was the same for all at any one time. However the physical electrode order, regular or inverted, depended on how each layer's drive electrodes connected to the rails, and did not have to be the same for all layers. Different physical configurations were used, the simplest, when all layers share the same electrode order, is shown at the top of Figure 3 for a five layer actuator. In this configuration each layer moved in the same direction and with the same velocity relative to the layer below it. Relative to the first stationary layer the second layer moved at a velocity of $F_{cyc}D_{pitch}$, the next layer moved at $2F_{cyc}D_{pitch}$, and so on. Because the speed increased with the number of layers, as $(N_{layer}\text{-}1)F_{cyc}D_{pitch}$, we term this configuration the speed configuration. The blocked force or toque was independent of layer number, as only the last layer pushes with a force equal to that of a non-stacked actuator, or approximately $N_{drop}W_{drop}\lambda$ [5], where N_{drop} is the number of drive droplets (330), W_{drop} is the individual drive droplet width of 0.9 mm, and λ is the surface tension of the oil/water interface, measured at 40 mN/m. A different 5-layer configuration is shown in bottom of Figure 3. In this configuration the physical electrode order alternated between regular and inverted as layers were added to the stack. As a result each layer moved in the opposite direction relative to the one below it. Relative to the base the odd (inverted electrode order) layers stayed stationary, while the even (regular electrode order) layers moved at a velocity of $F_{cyc}D_{pitch}$. Adding more layers in this configuration does not change the velocity, however each additional layer adds to the available force since all the layers push in unison. With only two layers the force is $N_{drop}W_{drop}\lambda$ but an added third layer also pushes the second layer from the top giving a three layer actuator a force of $2N_{drop}W_{drop}\lambda$. Since the force scaled as $(N_{layer}\text{-}1)N_{drop}W_{drop}\lambda$, we refer to this configuration as the force or torque configuration. Importantly the power available per layer was the same regardless of configuration since total layer capacitance, voltage, and frequency remain constant. Actuation movies for both configurations are available in supplementary material.

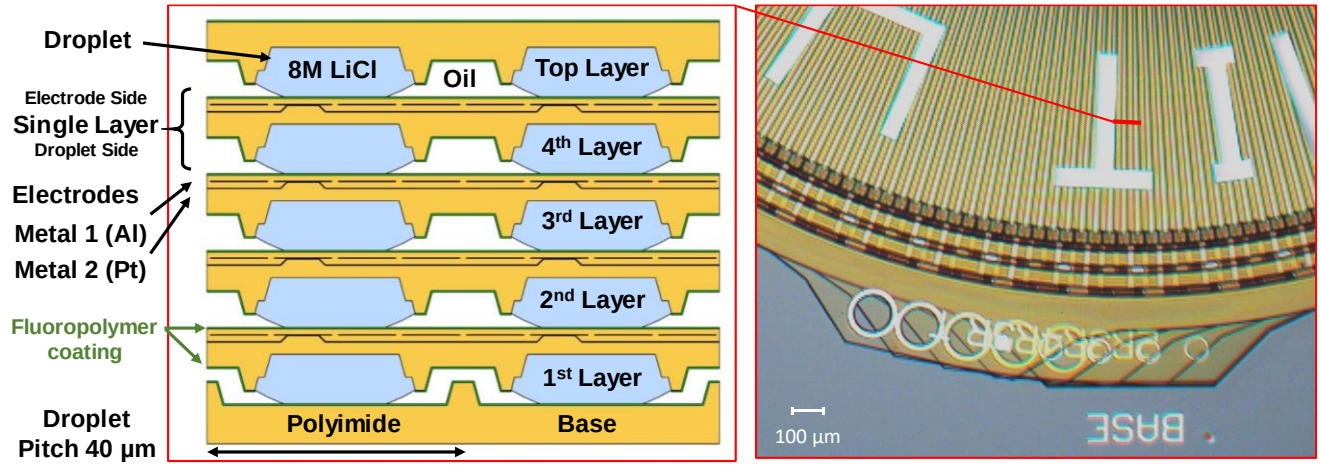

Figure 2. A cross sectional view (left) and a top down micrograph (right), of a stacked 5-layer microhydraulic rotational actuator. The first layer sits in a base and doesn't move, subsequent layers move by having the drive droplets glide on the fluoropolymer coating of the drive electrodes in the layers below. The layer tag numbers for layers 1-5 are 2R, 3R, 4R, 5R, T, from bottom to top. Layers 2-5R have inverted electrode order, with the final layer T displaying the MIT Logo text.

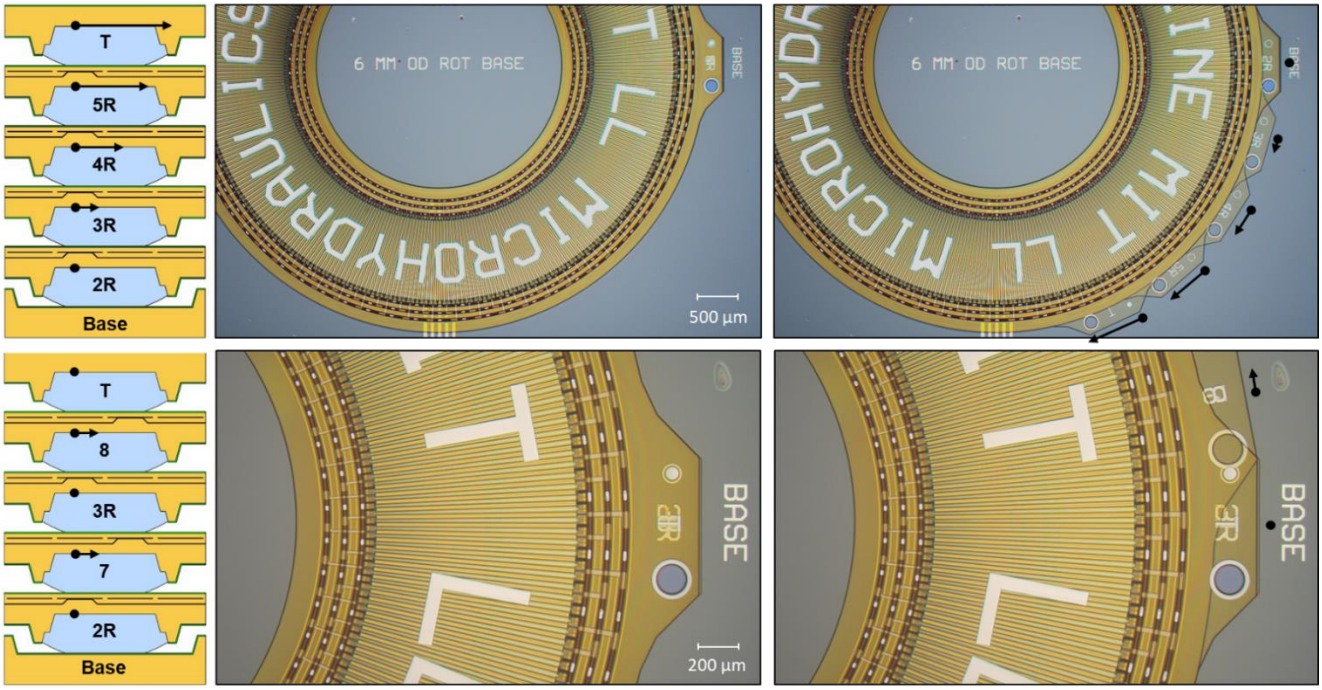

Figure 3. Images of 5-layer stack actuation in the speed (top) and force (bottom) configurations, left column also shows the cycle cross section profile for the corresponding configuration. Absolute velocity vectors are indicated for each layer with an arrow next to the layer tab. For the speed configuration (with layer order 2R, 3R, 4R, 5R, T) each subsequent layer moves with a fixed velocity ($F_{cyc}D_{pitch}$) relative to the layer below it. As a result the fifth layer (T) moves 4 times as fast as the second layer (3R). In the force configuration (with layer order 2R, 7, 3R, 8, T) each layer moves in opposite direction relative to the one below it. Relative to the base the odd layers (2R, 3R, T) remain stationary, while the even layers (7, 8) move at a uniform velocity ($F_{cyc}D_{pitch}$). Movies of these actuations are available in supplementary materials.

Actuation of a 5-layer linear actuator in a speed configuration is shown in Figure 4. These devices worked in a similar manner to the rotational actuators, and had W_{drop} of 2 mm, N_{drop} of 50, and D_{pitch} of 40 µm. The main operational difference was that unlike rotational actuators linear ones do not have an infinite stroke, and edge conditions at the end of the arrays are important. Since the droplet array should remain on top of the layer below at all times the effective stroke of these actuators was about 10 cycles in either direction. Figure 4b shows an actuator translation of 19 steps, one step short of the brush electrode pitch of 5 cycles. A movie of this actuator is available in supplementary material.

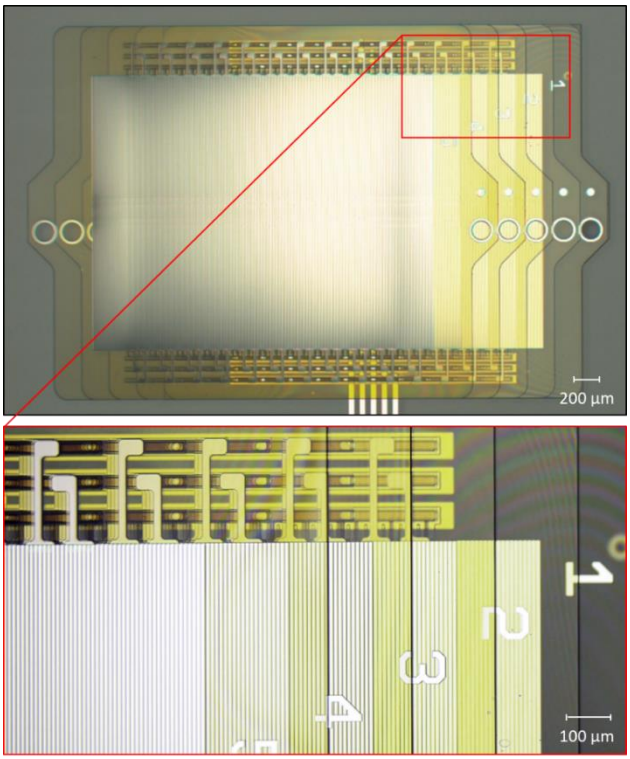

Figure 4. An image of a 5-layer linear microhydraulic actuator in the speed configuration. A movie of this actuation is available in supplementary materials.

2.3 METRICS

Using the moment arm length, R_{mean} of 2.2 mm, the blocked torque of a 5 layer actuator in the force configuration can be calculated as $(N_{layer}-1)R_{mean}N_{drop}W_{drop}\lambda$ = 0.11 mNm, giving a torque density of 78 Nm/kg. Angular velocity depended on the maximum cycle frequency, F_{max}, which in turn depended on the operating voltage. With a P1-4 voltage of 50 V and R voltage of -20 V, F_{max} was 2000 Hz. At higher frequencies the actuator occasionally skipped steps. Calculating the angular velocity as $F_{max}D_{pitch}$ gives 38 rad/s for the force configuration. For the 5 layer actuator in the speed configuration torque was $R_{mean}N_{drop}W_{drop}\lambda$ = 0.026 mNm, and the velocity was $(N_{layer}-1)$ $F_{max}D_{pitch}$ = 152 rad/s. At maximum frequency the actuator accelerated to full velocity in a single step, or in less than 0.125 ms, which corresponds to an angular acceleration over 0.3 Mrad/s^2 for a 2 layer actuator and 1.2 Mrad/s^2 for a 5 layer actuator. A movie of an actuation at F_{max} for a 2 layer rotational actuator is available in supplementary material. Maximum output power for either configuration was approximately $¼F_{max}D_{pitch}N_{drop}W_{drop}\lambda(N_{layer}-1)$ [5], and when normalized by mass gives 0.74 kW/kg output power density, similar to inductive motors.

3. DISCUSSION

3.1 ARBITRARY CONFIGURATIONS

The speed and force configurations demonstrated in the previous section are only a subset of possible layer arrangements. In general a multilayer stack can consist of M regular, and M inverted electrode order layers, alternating up through the actuator. For M=1 this results in the force configuration, shown for a linear actuator in Figure 5a, but for M=2, shown in Figure 5b, the actuator has twice the speed at half the force of the M=1 configuration. Generally, for any M configuration the actuator will have 1/M force and M speed of the force (M=1) configuration. Such design flexibility allows for a tailored speed vs power profile, without the use of gears. This is particularly important for microactuation, where gearing can be difficult, inefficient, and consume a significant amount of the size, weight, and power budget.

3.2 TORQUE AND SPEED SPACE

Although microhydraulic rotational actuators with the droplet pitch shown in this paper have a similar power density to inductive motors, when power is broken down to torque and speed a significant difference become apparent. Figure 6 shows the maximum unloaded speed, plotted against the blocked torque density, for our actuators, for selected high-performance inductive motors, and for biological joints. Inductive motors have a high speed and low torque density, while microhydraulic actuators and biological joints have much higher torque density at a lower speed. The gap can be bridged by using different configurations, but a configuration with M over 100 is required to reach the speeds of high-performance inductive motors. The fact that microhydraulic actuators reside in the same region of the torque/speed diagram as biological joints, but are significantly better in both metrics, suggest robotic and micro-robotic applications. Many robotic systems use inductive servos that have a high gear ratio to provide higher torque. Microhydraulic actuators would not need gears, and as such could be made more compact and responsive. For example, fabricating a robotic human-like hand is very difficult for current actuator technology, partly due to the lack of space in the fingers for an inductive motor and gears. High torque microhydraulic actuators could be the solution. Also it is important to point out that microhydraulic actuators can be improved greatly by scaling dimensions, while inductive motors get worse when scaled down. For a droplet pitch of 15 μm the projected power density is an order of magnitude greater than high-performance inductive motors at a very high torque density, as shown in Figure 6.

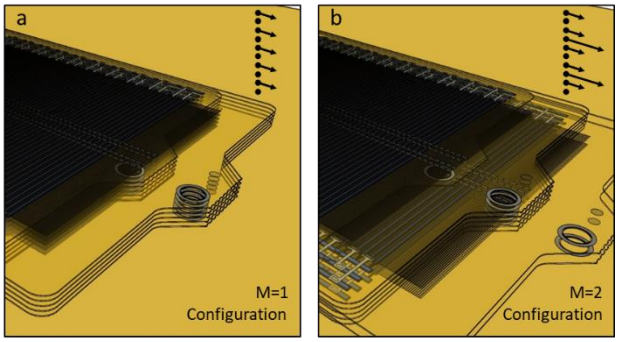

Figure 5. A diagram of two configuration with M=1 ***(a)****, and M=2* ***(b)****. For any value of M, the stacking order will alternate with M forward going layers stacked on top of M backward going layers. Absolute velocity vectors are also shown. In general, any M configuration will have M maximum velocity and 1/M force density of the M=1 or force configuration.*

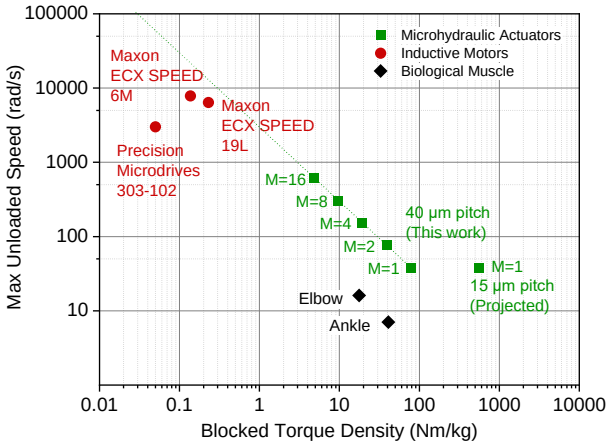

Figure 6. A plot of maximum unloaded rotational velocity and blocked torque density for various rotational actuators. Inductive motors tend to have a high speed at low torque density, while microhydraulic motors and biological joints tend to have a low velocity and a high torque density. Different M configuration can exchange speed for torque. 40 µm droplet pitch devices are shown in this work, while 15µm droplet pitch devices are projected from scaling trends. Metrics for the Microdrive 303-102 motor were measured in our laboratory, Maxon motor metrics were taken from online data sheets. Elbow and ankle measurements were obtained from the first author using a load cell and a gyroscope, and are typical of biological muscle performance. Normalization masses for muscle torque calculations were the arm mass below the shoulder, and the leg mass below the knee.

3.3 LIQUID INTERCONNECT

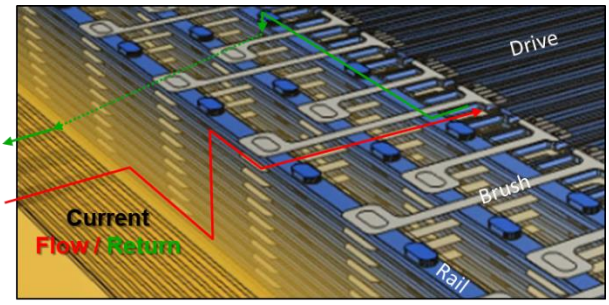

Name	Unit	Drive	Brush	Water
Material Type		Al	Pt	8 M LiCl
Resistivity	Ω-m	9.0×10^{-8}	2.0×10^{-7}	6.6×10^{-2}
Thickness	m	6.0×10^{-8}	1.0×10^{-7}	5.5×10^{-6}
Resistance [(a)]	Ω	300	16	1.6×10^{5}
Capacitance	F/m^2	2.7×10^{-5}	0.17	From Al or Pt to water 8 M LiCl
Area [(a)]	mm^2	8.0×10^{-2}	5.7×10^{-4}	
Capacitance [(a)]	pF	2.16	96.9	

(a) Worst case, per single brush electrode

Figure 7. A diagram showing the electrical power distribution network for a linear multilayer microhydraulic actuator. Alternating current flows from the base up through the fluidic rails and vias, to the brushes, then to the drive electrodes. It then couples to the drive droplets in the layer above and returns through the fluidic rails and vias back to the base. Driving (Al) electrodes are shown in black, brush (Pt) electrodes are shown in gray, and liquid interconnect components (water 8M LiCl, rails, droplets, and vias) are shown in blue. The table shows the measured network parameters with resistance and capacitance normalized to a subunit of the actuator containing a single brush electrode.

Electrical power had to be connected to all microhydraulic layers, even though they move relative to each other. This could be done capacitively [13] for some configurations, but in this work a liquid interconnect was used [18,19]. The electrical power delivery path in the actuator is outlined in Figure 7. Signals enter from the connector to the Al interconnect at the base, connect with a metal via to the Pt base brush electrodes, capacitively couple to the water 8M LiCl rails through an electrical double layer, ionically conduct through the fluidic rails and vias to Pt brush electrodes in each layer, transfer through a metal via to the Al drive electrodes, couple capacitively to the drive droplets to form the electrowetting capacitor, then return though the 8 M LiCl reference rail into the R Pt brush electrodes in the base, and return to the connector. This complex path requires that no double layer in the system exceeds the electrolysis voltage of 1.2 V, thus the areas and capacitances of the double layers used for the Pt-liquid connection are critical. The table in Figure 7 shows the measured electrical parameters of the interconnect network. The double layer capacitance per area was high at 0.17 F/m^2, and thus the absolute double-layer capacitance was approximately 50 times higher than the electro-wetting capacitance. Such a capacitive ratio kept 98% of

the applied voltage across the electrowetting dielectric, and prevented electrolysis at the Pt brush electrodes. Electrolysis did occur if two phases somehow shorted to each other. Resistance was another potential issue. Even though water with 8M LiCl is a relatively low resistance ionic conductor, it is still over 5 orders of magnitude more resistive than a typical interconnect metal, making it the predominant resistive component in the network. Ionic resistivity, however, did not limit actuator performance, as the resistive-capacitive product was 0.34 μs, and thus much shorter than the minimum stepping time of 125 μs.

3.4 CHALLENGES

Microhydraulic technology has unique challengers due to its fluidic nature, and reliance on unsupported thin films. Layers had to be low stress not to curl or warp. Careful optimization of the polyimide anneals was required make the radius of curvature for individual layers greater than 10 cm. Fluidic challenges included evaporation and contamination. Evaporation of the water phase was controlled by adding 8 M LiCl. LiCl, being highly deliquescent, prevents the water from evaporating at an ambient of 20°C and 50% relative humidity. As a matter of fact we have a μL size droplet of water with 8 M LiCl in our lab, exposed to the ambient, that has remained unchanged for over 3 years. The dodecane used for the oil phase does evaporate slowly from the actuator bath, and had to be replenished every few days. In the future, a packaging solution will be required to keep the actuator liquids contained. Impurities in the fluids are also a concern. Molecular impurities, even at low concentrations, can disturb the surface tension and effect actuator performance. To avoid molecular impurities, clean components and fluids were used. Macro-particles of various sizes were an even bigger challenge. Liquid-air interfaces of the droplets exposed during wetting, pressurization, release, and assembly tend to readily grab particles out of the atmosphere and were impossible to clean with techniques we tried. During operation, smaller particles tended to scratch the surface of the electrodes and eventually lead to actuator failure, and particles larger than 10 μm often prevented the actuator from working completely by bridging droplets, and shorting phases. To suppress particle issues the entire process flow occurred in a clean room. Never the less, particles were still the leading cause of yield failure.

4. MATERIALS AND METHODS

Actuator fabrication consisted of over 90 steps listed in detail in the supplementary materials. Below is the summary of the fabrication flow divided into two consecutive parts, traditional silicon wafer based MEMs processing, followed by custom micro-hydraulic processing.

4.1 PART 1: WAFER-BASED PROCESSING

The first part of fabrication, outlined in Figure 8a-f, took place in a 200-mm silicon wafer fabrication facility (MIT Lincoln Laboratory's Microelectronics Laboratory). In general actuators were fabricated from the electrode side to the droplet side, except for the electrowetting fluoropolymer which was custom processed last. Fabrication started with cleaned silicon wafers, which were coated with polyimide (Low stress PI2611, Dupont), and cured to give a 1.1 µm thick film. The drive electrode metal (60 nm Al) was then deposited, patterned, and etched to form the drive electrodes, as shown in Figure 8a. The interlayer dielectric of 0.9 µm polyimide was spun on and cured. The via layer was then patterned and etched into the polyimide, as shown in Figure 8b. Next the brush electrode metal lithography was performed, the metal deposited (100 nm Pt), and patterned with a lift-off process, as shown in Figure 8c. After metallization, two layers of 4.2 µm thick polyimide were spun on and cured. Next the droplet wall was patterned and etched with a timed etch 3.6 µm into the polyimide, as shown in Figure 8d. Following the wall etch, the overall outline of the microhydraulic layer, including the fluidic vias, was patterned in a 16 µm resist. The outline was etched just 1.5 µm short of the silicon-polyimide interface, Figure 8e. This etch was critical, as the thinned regions of polyimide must be less than 2 µm to be properly etched in the next section, and more than 1 µm to not rip during the peel process. Next the regions between die, were patterned and die streets were etched all the way to the silicon interface. Finally the polyimide was coated with a 20 nm film of fluoropolymer (Cytop Type A, Asahi Glass Co.), cured, and patterned with the hydrophobic resist pattern, as shown in Figure 8f. Importantly the hydrophilic pattern included all the regions in the outline pattern, so when the hydrophilic etch was done in the next section it fully separated the parts in the outline regions and formed the fluidic vias.

4.2 PART 2: DIE-BASED PROCESSING

Subsequent processing was done on custom built tools in the microfluidics laboratory on individual wafer die. After cleaving the wafer, each polyimide die was peeled off, as shown in Figure 8g. Peeling stopped 2 mm from the end of the die leaving it partly attached to the silicon. A fluoropolymer solution (Cytop Type A, Asahi Glass Co., 0.6% in FC40, Sigma-Aldrich) was then injected into the peeling front, and the polyimide film was laid back down and then lifted again to wet the back with fluoropolymer. A video of this process is available in the supplementary section. After the layer was lifted again excess fluoropolymer solution was drained, and the fluoropolymer film annealed. The process was repeated with a second fluoropolymer (1% FluoroPel, Cytonix). Two fluoropolymer coats are required because FluroPel did not adhere to polyimide, and Cytop Type A did not electrowet properly. A sequential combination of

the two resulted in a 14 nm film with acceptable adhesion and excellent electrowetting. Once both coats were applied and annealed, the polyimide layer was completely peeled and removed from the silicon die, and the silicon die was plasma etched to remove the fluoropolymer. Once the silicon die was free of fluoropolymer, the peeled edge of the polyimide film was placed back in the original position. Refined bees wax (Sigma Aldrich) was melted into the interface between the wafer and the polyimide film, and the film was laid down for the third and final time. A video of this process is also available in the supplemental section. At the end of the peel process the polyimide film has an electrowetting fluoro-polymer added to the electrode side, and a thin layer of release wax separating the silicon and the fluoro-polymer. The die was then etched to remove the final 2 μm of polyimide from the layer outline and from the fluidic vias of the layers, as well as to remove the fluoropolymer from the exposed hydrophilic droplet regions. Resist was then stripped in acetone, and the layers were wetted with a solution of water 8 M LiCl. Each rail was then pressurized with a micro-pipette (TIP10TW1-L, World Precision Instruments) attached to a monometer to a pressure of 12 cm of 8M LiCl. Pressurization gave the droplets a well-defined curvature, as shown in Figure 8h. After wetting and pressurization, individual microhydraulic layers were lifted off the wax by attaching a small piece of tape to the tab (kapton tape with silicone adhesive). The tape adhesive and any residual wax was removed by cleaning in decane and dodecane. A fully released microhydraulic layer is shown in Figure 8i.

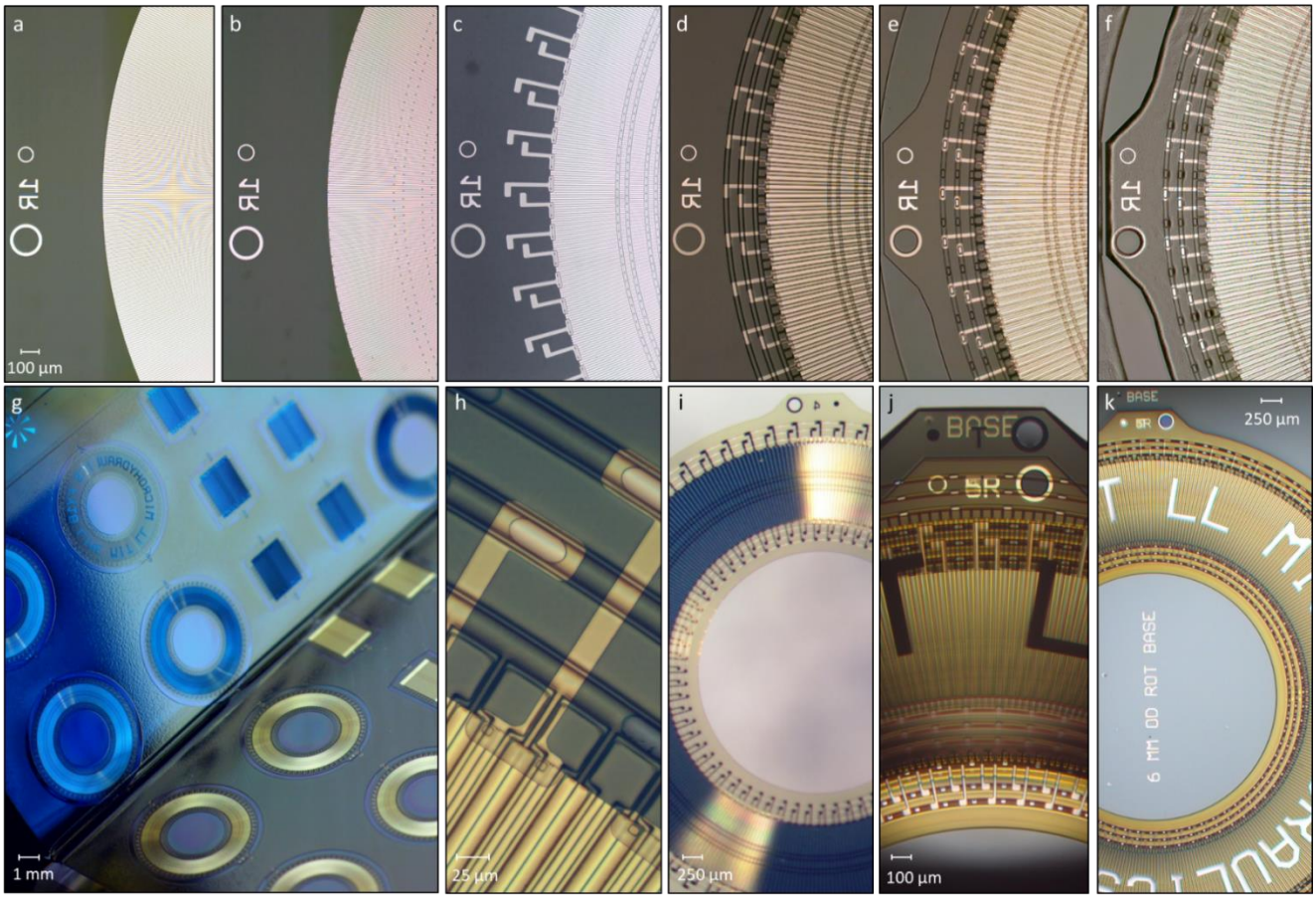

*Figure 8. Images of the multilayer microhydraulic actuator at various stages of fabrication. Top row shows the wafer based processing for all major lithography steps: Al metal **(a)**, metal via **(b)**, Pt metal **(c)**, droplet wall **(d)**, outside and die etch **(e)**, and hydrophilic patterning **(f)**. Bottom row shows the major custom microhydraulics steps: the peel and laydown for electrowetting fluoropolymer coating and the addition of release wax **(g)**, droplet wetting and pressurization **(h)**, layer release **(i)**, actuator assembly **(j)**, and the finished actuator in a testing dodecane bath **(k)**. Peel and wetting videos are available in supplementary materials.*

Before assembly the base layer was removed from the silicon wafer and transferred onto a clean glass slide to minimize parasitic capacitances. A drop of oil was placed on the base and the first microhydraulic layer was aligned and pushed into position. This operation was done with the layer at a small angle, approximately 10° to the base horizontal plane. As the layer was pushed off the aligner it gently folded onto the base. Once it was sufficiently close, it self-aligned due to surface tension forces. Each subsequent layer was assembled the same way, as show in the final step of a 5 layer assembly in Figure 8j. Before testing each rail was pressurized to a Laplace pressure of 24 cm of 8 M LiCl using a micropipette through the top fluidic vias. The actuator was then placed in a dodecane bath for testing, as shown in Figure 8k. Testing was done using a National Instruments PXI system, customized with a bank of high voltage amplifiers.

5. CONCLUSION

Multilayer microhydraulic actuators demonstrate a unique combination of key concepts which enable precise, high-power, low-voltage capacitive actuation. Layering allows for a large actuation volume with low-voltage at each layer. Stepping allows for high-force and power, as well as a fine digital resolution of motion. Different configurations of layers allow for actuators with multiple speed and force profiles, without the use of gears. In a high force configuration, multilayer microhydraulic actuators have a torque density that far exceeds inductive motors and is significantly greater than biological joints. High torque density results in fast reaction time, with the actuators able to accelerate to full power and speed in less than 125 μs. These characteristic make multilayer microhydraulic actuators particularly well suited for robotics, where fast reactions to a dynamic environment are important. Our technology may excel particularly well at the small scale where inductive motors are inefficient, and find use in small robotic joints, microrobotics, robotic surgery [23], and programmable materials [24].

6. ACKNOWLEDGEMENTS

The authors thank Prof. Sangbae Kim for his insights into robotic applications of microhydraulics. Thanks also to Dr. Shaun Berry, and Dr. Mordechai Rothschild for helpful discussions, and the Microelectronics Laboratory engineering and operation staff for their invaluable assistance during process development and fabrication. This material is based upon work supported by the Under Secretary of Defense for Research and Engineering and Defense Advanced Research Projects Agency under Air Force Contract No. FA8702-15-D-0001. Any opinions, findings, conclusions or recommendations expressed in this material are those of the authors and do not necessarily reflect the views of the Under Secretary of Defense for Research and Engineering and Defense Advanced Research Projects Agency.

REFERENCES

[1] Fan, L. S., Tai, Y. C., & Muller, R. S. IC-processed electrostatic micro-motors. Technical Digest, International Electron Devices Meeting, San Francisco, CA, USA, 666 (1988).

[2] Kumada, A. A Piezoelectric Ultrasonic Motor. 1985 Jpn. J. Appl. Phys. 24 739 (1985).

[3] Hirata, H. & Ueha, S. Design of a traveling wave type ultrasonic motor. IEEE Transactions on Ultrasonics, Ferroelectrics, and Frequency Control. 42, no. 2, 225-231 (1995).

[4] Morita, T. Miniature piezoelectric motors. Sensors and Actuators A: Physical. 103, 3, 2003, 291 (2003).

[5] Kedzierski, J., & Holihan, E., Linear and rotational microhydraulic actuators driven by electrowetting. Science Robotics. 3, 22 (2018).

[6] Basha, M. A., Safavi-Naeini, S. & Chaudhuri S. K. Design and Fabrication of an Electrostatic Micromotor with a Low Operating Voltage. TRANSDUCERS 2007 - 2007 International Solid-State Sensors, Actuators and Microsystems Conference, Lyon, 2007, 1139 (2007).

[7] Livermore, C., Forte, A. R., Lyszczarz, T., Umans, S. D., Ayon, A. A. & Lang, J. H. A High-Power MEMS Electric Induction Motor. Journal of Microelectromechanical Systems. 13, 465 (2004).

[8] Penskiy, I. & Bergbreiter, S. Optimized electrostatic inchworm motors using a flexible driving arm. Journal Micromech. Microeng. 23 015018 (2013).

[9] Yeh, R., Hollar, S. & Pister, K. S. Single mask, large force and large displacement electrostatic linear inchworm motors. Journal Microelectromechanical Systems. 11, 330 (2002).

[10] Wood, R. J. & Clarke, D. R. Multilayer Dielectric Elastomers for Fast, Programmable Actuation without Prestretch. Advanced Materials. 28, 8058 (2016).

[11] Takahashi, S. Multilayer Piezoelectric Ceramic Actuators and Their Applications. Jpn. J. Appl. Phys. 24 41 (1985).

[12] Kellaris, N., Venkata, V. G., Smith, G. M., Mitchell, S. K. & Keplinger, C. Peano-HASEL actuators: Muscle-mimetic, electrohydraulic transducers that linearly contract on activation. Science Robotics. 3 (2018).

[13] Kedzierski, J., Holihan, E., Cabrera, R. & Weaver, I. Re-engineering artificial muscle with microhydraulics, Microsystems and Nanoengineering. 3, 17016 (2017).

[14] Zhao, Y. P. & Wang, Y. Fundamentals and applications of electrowetting: A critical review. Rev. Adhesion Adhesives. 1, 114 (2013).

[15] Berry, S., Kedzierski, J. & Abedian, B. Low voltage electrowetting using thin fluoroploymer films. Journal Colloid Interface Sci. 303, 517 (2006).

[16] Takei, A., Khiem, N. B., Iwase, E., Matsumoto, K. & Shimoyama, I. Liquid motor driven by electrowetting, MEMS 2008: 42-45. (2008)

[17] Kedzierski, J., Meng, K., Thorsen, T., Cabrera, R. & Berry, S. Microhydraulic Electrowetting Actuators. Journal of Microelectromechanical Systems. 25, 394 (2016).

[18] Suarez, F. et al. Flexible thermoelectric generator using bulk legs and liquid metal interconnects for wearable electronics. Applied Energy, 202, 736 (2017).

[19] Park, C. W. et al. Photolithography-Based Patterning of Liquid Metal Interconnects for Monolithically Integrated Stretchable Circuits. ACS Applied Materials & Interfaces. 8, 24, 15459 (2016).

[20] Ashurst, W.R., Carraro, C. & Maboudian, R. Vapor phase anti-stiction coatings for MEMS. IEEE Transactions on Device and Materials Reliability. 3, 4, 173 (2003).

[21] Zhang, W. M., Yan, H., Peng, Z. K. & Meng, G. Electrostatic pull-in instability in MEMS/NEMS: A review. Sensors and Actuators A: Physical. 214, 187 (2014)

[22] Srinivasan, U., Liepmann, D. & Howe R. T. Microstructure to Substrate Self-Assembly Using Capillary Forces. Journal of microelectromechanical systems. 10, 17 (2001).

[23] Le, H. M., Do T. N. & Phee, S. J. A survey on actuators-driven surgical robots. Sensors and Actuators A: Physical. 247, 2016, 323 (2016).

[24] Toffoli, T. & Margolus N. Programmable Matter: Concepts and Realization. Physica D. 47, 263 (1991).